Graphene as an Electrode for Solution-Processed Electron-Transporting Organic Transistors

Subir Parui[†,*], *Mário Ribeiro*[†], *Ainhoa Atxabal*[†], *Roger Llopis*[†], *Fèlix Casanova*[†,‡], *Luis E. Hueso*[†,‡,*]

[†]CIC nanoGUNE, 20018 Donostia-San Sebastian, Basque Country, Spain

[‡]IKERBASQUE, Basque Foundation for Science, 48013 Bilbao, Basque Country, Spain

*E-mail: s.parui@nanogune.eu; l.hueso@nanogune.eu

ABSTRACT:

Organic field-effect transistors (OFETs) are fundamental building blocks for plastic electronics such as organic photovoltaics or bendable displays with organic light emitting diodes, and radio-frequency identification (RFID) tags. A key part in the performance of OFET is the organic material constituting the channel. OFETs based on solution-processed polymers represent a new class of organic electronic devices. Recent developments in upscale solution-processed polymers have advanced towards high throughput, low-cost, and environmental friendly materials for high-performance applications. Together with the integration of high performance materials, another enduring challenge in OFET development is the improvement and control of the injection of the charge carriers. Graphene, a two-dimensional layer of covalently bonded carbon atoms, is steadily making progress into applications relying on van der Waals heterointerfaces with organic semiconductors. Here, we demonstrate the versatile operation of solution-processed organic transistors both in lateral and vertical geometry by exploiting the weak-screening effect and work function modulation properties of the graphene electrodes. Our results demonstrate a general strategy for overcoming traditional noble metal electrodes, and to integrate graphene with solution-processed Polyera ActiveInk™ N2200 polymer transistors for high-performance devices suitable for future plastic electronics.

KEYWORDS: Graphene, solution-processed polymer, energy barrier, organic field-effect transistor

Organic field-effect transistors (OFETs) are fundamental building blocks for complex plastic electronic devices, such as organic photovoltaics (OPVs) panels or bendable displays with organic light emitting diodes (OLEDs).[1,2] A key part in the performance of OFETs is the organic material constituting the carrier channel. In this respect, recent developments in upscale solution-processed polymers have advanced towards high throughput, low-cost, and environmental friendly organic materials for industrial applications.[3-5]

Together with the integration of high performance materials, an enduring challenge in OFET development is the improvement and control of the injection of the charge carriers into the organic layer.[6] The carrier injection is performed by the source and drain (S, D) contact electrodes and generally noble metals are used due to their chemical stability in ambient condition and closely matching work function with the orbital levels of many semiconducting polymers. However, noble metals suffer from a series of drawbacks that make the search for alternative electrodes a pressing demand. On the one hand, metals have a large density of electronic states (DOS), which makes any modulation of their work function with an external electric field extremely challenging. On the other hand, gold (Au), a commonly used electrode to date, is also increasingly expensive for the production of organic devices,[7] whose ultimate goal is to be low-cost, light weight, and with performances comparable to benchmark inorganic devices.

Graphene, a two-dimensional layer of covalently bonded carbon atoms,[8] is steadily making progress into applications relying on heterointerfaces with both organic and inorganic semiconductors.[9-20] The increasing availability of atomically flat chemical vapor deposition (CVD)-grown monolayer graphene makes it a suitable candidate to circumvent the obstacles presented above by noble metals, while introducing new device functionalities. Although the

lack of bandgap in graphene undermines its potential for logic applications,[21] hybrid structures of graphene and organic semiconductors are being considered as next-generation electronic devices.[13,14,20,22-24] The most important characteristics of monolayer graphene that can be exploited in organic transistors are its gate tunable work function,[25] its weak electrostatic screening,[26] and its chemical stability. Electrostatic gating can change the work function of graphene from 4.4 to 4.8 eV,[25] values that closely match those of many metallic electrode materials.[27,28] In the same regard, the weak electrostatic screening of graphene emerges from its low DOS and ultimate thinness. This property allows the applied gate electric field to penetrate through the graphene layer and to modulate the energy levels of the organic semiconductor on top of it, an effect unattainable by any uniformly grown metallic electrode. Additionally, the chemical stability of graphene allows for the *ex-situ* fabrication of the devices with virtually no detrimental damage to its electrical properties. Graphene embodies then a set of characteristics that suit the role of electrode for organic transistors.

For our proof-of-concept devices we use Poly{[N,N' -bis(2-octyldodecyl)-naphthalene-1,4,5,8-bis(dicarboximide)-2,6-diyl]-alt-5,5' -(2,2' -bithiophene)} (P(NDI2OD-T2)), also known as Polyera ActiveInk™ N2200, which has generated substantial interest in the worldwide scientific community,[4,5,29-32] as an electron-transporting channel material. It is a highly soluble, air stable polymer that has an optical gap of only ~1.45 eV, with its lowest unoccupied molecular orbital, LUMO, and its highest occupied molecular orbital, HOMO, energy levels ~4.0 eV and ~5.6 eV below the vacuum level, respectively.[4] The naphthalene-bis(dicarboximide) core in this polymer ensures a strong electron-depleted electronic structure and a regioregular and highly π-conjugated polymeric backbone.[4] The field-effect electron mobility in this material at room-

temperature has been demonstrated to vary from ~6 × 10^{-3} cm^2/Vs to ~0.85 cm^2/Vs, depending on the device configuration.[4,31]

Here, we demonstrate the versatile operation of solution-processed organic transistors by exploiting the weak-screening effect and work function modulation properties of the graphene electrodes. We use a heterojunction of CVD-grown graphene and Polyera ActiveInk™ N2200 for studying the electron transport in lateral and vertical organic field-effect transistors (LOFET and VOFET, respectively). Our design for both lateral and vertical transistors allows us to monitor in-device the electrical properties of the graphene electrodes at each stage of the fabrication step, in particular the modulation of graphene's Fermi level, and the weak-screening contributions with applied gate electric field. More importantly, our results demonstrate a general strategy for overcoming traditional noble metal electrodes, and to integrate two-dimensional graphene electrodes with solution-processed electron-transporting (n-type) organic transistors for high-performance lateral and vertical device architectures. Therefore, light-weight, environment friendly and low-cost graphene-based organic devices will be realized for numerous applications in next-generation plastic electronics.

RESULTS AND DISCUSSION

Figure 1(a) and 1(b) show the sketch of the graphene/N2200/graphene-based conventional LOFET and graphene/N2200/Al-based VOFET, respectively. The fabrication steps are explained in detail in the methods section. For the lateral transistor, we use two 100-μm-wide graphene stripes as source and drain electrodes. The shortest distance between the two graphene electrodes and the length of each graphene stripe provide the channel length, L = 15 μm, and channel width,

W = 1.5 mm, (W/L = 100) for the LOFET. For both lateral and vertical transistors, a 90-nm-thick layer of N2200 is spin-coated after HMDS vapor-priming of the substrate. The 90-nm-thick N2200 layer, confined in between a 20-μm-wide graphene stripe and a 300-μm-wide Al bar, acts as the channel length for the vertical transistor. The chemical structure of the N2200 polymer is illustrated in Figure 1(c). Figure 1(d) presents the optical microscopy image of a LOFET, with the graphene stripes indicated inside the dotted lines. The atomic force microscopy image of the surface topography of the spin-coated N2200 polymer on top of graphene, shown in Figure 1(e), exhibits a uniform N2200 film with surface roughness of ~ 1 nm.

We start by evaluating the lateral configuration, as it is the most common template for the analysis of electrical transport properties and it is widely used in current plastic-based electronics. In order to monitor the changes that the graphene electrodes undergo during the fabrication process, we report the change in graphene resistance with respect to the gate voltage sweep after electrode-shaping, after HMDS vapor priming, and after spin coating the N2200 polymer on top of graphene. Figure 2(a) and 2(b) show the room temperature graphene field-effect characteristics of the two graphene stripes that are used as source and drain (S, D) electrodes, respectively, for the LOFET. We measure the change in graphene resistance by contacting the Ti/Au contacts at the two ends of each graphene strip (2-probe current-voltage method) and varying the gate voltage V_G. From the dependence of the graphene resistance versus V_G, we find that both graphene electrodes (S and D) are hole-doped, with charge neutrality point (CNP) at positive gate voltages of 44 V and 41 V, respectively. The hole-doping is common when CVD-grown graphene is transferred onto a Si/300-nm-thick SiO_2 substrates.[14] Furthermore, we introduce HMDS vapor priming to perform SiO_2 surface-passivation, which has been established to improve n-channel OFET activity.[2,31] In both stripes, the CNP of the

graphene electrodes shifts more than 20 V, appearing at 67 and 64 V, respectively. The graphene resistance at CNP and the curvature of the peak remain unchanged after HMDS vapor priming, indicating that other properties of graphene apart from the doping remain consistent. The addition of a 90-nm-thick layer of N2200 shifts the position of the CNP to higher V_G (approximately 90 V). This increment is due to the formation of an electrical dipole at the graphene/N2200 interface, arising from the transfer of electrons from graphene to N2200. The decrease in resistance at CNP by 10-16 % for both electrodes and the broadening of the curvature of the peak suggest the formation of an extra channel of conduction, decreasing of the effective charge carrier mobility in graphene. We determined the surface charge carrier mobility of pristine graphene to be higher than 3000 $cm^2V^{-1}s^{-1}$ at RT. We extract the mobility at a specific carrier density of ~10^{12} cm^{-2} at the deflection point.[14]

Moving to the transport across the solution-processed N2200 polymer, the output characteristics of the graphene contacted LOFET are shown in Figure 2(c) at RT and 2(d) at 100 K, respectively. We observe nearly ideal output characteristics for the transistor operating at RT. The linear $I_D - V_D$ relationship at low V_D voltage region indicates a nearly ohmic contact between the graphene and N2200 polymer. However, at 100 K, a sharp non-linear increase in $I_D - V_D$ curves over a wide V_D voltage reflects the existence of stronger contributions from interface-dominated transport, which might impose a bound on the charge-carrier mobility of N2200 at very low temperatures. Figure 2(e) shows the transfer characteristics of the N2200-graphene based LOFET measured both at room temperature and at 100 K. The device exhibits typical n-type transistor behavior with RT on/off current ratio over six orders of magnitude. In Figure 2(f), we estimate the electron mobility to be 1.06×10^{-2} at RT and 2.37×10^{-5} cm^2/Vs at 100 K respectively from the slope of $\sqrt{I_D}$ versus V_G plot in the saturation regime. In control experiments

(see supplementary information), we found the electron mobility of N2200 to be ~ (5.5 ± 0.5) × 10^{-3} cm^2/Vs at RT from transistors with Au electrodes as also reported in literature.[31] The LOFETs with graphene electrodes exhibit charge carrier mobility nearly 2 times of magnitude better than the corresponding LOFET mobility obtained with conventional 30-nm-thick Au electrodes in similar bottom-contact, bottom-gate device configuration. In this proof-of-concept device we have found a much superior performance using graphene as electrode material for electron-transporting organic channel. Thus, we conclude that graphene can be used as source/drain contacts not only for hole-transporting semiconductors[7,16,33] but also for electron-transporting semiconductor to improve the performance of organic transistors.

We now turn our attention to the vertical operation of the graphene/N2200 junction. Field-effect transistors using vertical configurations are steadily making progress into electronic devices, principally since they reduce energy consumption and occupy much less space when compared to its traditional lateral counterparts.[34-42] Again, we assess the impact of the different processes in the transfer curves of the graphene electrode.

Figure 3(a) shows the RT field-effect characteristics of the graphene source electrode that is used for the VOFET device. The resistance of the graphene channel is higher in this case when compared to the lateral devices since we have used a narrower graphene stripe (20 μm wide). However, the shift in the position of graphene CNP remains consistent with the earlier LOFET graphene electrodes. To demonstrate the vertical field-effect transistor behavior, Figure 3(b) presents the I_D - V_G characteristics at RT of the graphene/N2200 (90-nm-thick)/Al-based VOFET for several positive V_D. The reverse biased graphene/N2200 junction provides the maximum modulation of the drain current. The transistor switches from the ‘off’ state to the ‘on’ state when

V_G is varied from -50 V to 90 V, showing a maximum on/off current ratio greater than three orders of magnitude at V_D = 2 V (see the inset of figure 3b). Overall, the current on/off ratio can be divided into two distinct regimes depending on the applied drain voltage. The best measured 'off' state current that is lower bound by the gate leakage current is as low as ~10^{-12} A in our device. However, the 'on' current is determined by the N2200 channel conductivity. Thus the current on/off ratio starts to increase initially with increasing V_D as the channel conductivity increases rapidly compared to the gate leakage current. However, after a certain electric field the diode leakage current contributes and the current on/off ratio stats to decrease providing its peak value at $V_D \approx 2$ V. We notice that the effective turn-on gate voltage at which the transistor switches from 'off' state to 'on' state is stable around -30 V for all the measurements. These reproducible characteristics are suitable for many applications. Interestingly, and as a direct consequence from the observations shown in the previous figure, the VOFET operates in the gate voltage range of ± 30 V whereas the CNP of graphene appears to be at much higher gate voltage of ~99 V. Since the modulation of the Fermi energy level depends with the square root of the carrier density, the rate of change of the Fermi energy with V_G will be lower for higher doping. The device operation this far from the CNP indicates then the main contributing mechanism to the vertical operation is the weak field screening of graphene, which allows the electric field to reach the N2200 polymer and enables the VOFET operation.[42] In this case, the tunneling current at the graphene/N2200 interface plays a strong role for transistor behavior. We carried out temperature dependent measurements that can be seen in Figure 3(c) in the temperature range from 295 K to 205 K and at V_D = 6 V. The 'off' state current decreases with decreasing temperature and so does the 'on' state current, although to a minor degree. The inset of figure 3(c) shows the associated on/off current ratio increases with decreasing temperature. All these

features are the consequence of the competition between tunneling (under the barrier) and thermionic (over the barrier) transport at different bias voltages and at different temperatures. For a clearer picture on these mechanisms, a temperature dependence of the transfer and output characteristics allow us to draw quantitative conclusions regarding the nature of the energy barrier and energy level bending.

Figure 4(a), 4(b), and 4(c) illustrate the mechanisms of formation of the energy barrier between the graphene electrode and the organic semiconductor. Applying a gate electric field can modulate not only the height of the barrier but also the energy level bending in the semiconductor due to weak-screening effects of graphene. In figure 4(b), a negative gate voltage can hardly induce any charge carrier in the n-type N2200 polymer, leading the electrons to flow over the barrier in a thermionic emission process. Positive gate voltage, as seen in figure 4(c), shifts the graphene Fermi level upward and also induces the accumulation of electrons in the N2200 polymer close to the interface with graphene. This will bend the energy levels and promote tunneling through the interface-barrier from graphene to the LUMO level of N2200.

Figure 4(d) represents an output curve of the vertical junction diode in the semi-log scale at RT. The drain current at the positive side of V_D shows a large modulation with respect to V_G, while the current modulation at the negative side of V_D is quite small. As the LUMO and HOMO of N2200 are ~4.0 and ~5.6 eV respectively, the electrical transport occurs between the LUMO of N2200 and the Fermi energy level of graphene (~4.4 to 4.8 eV). The large current modulation at the positive side of V_D indicates a strong gate-modulation of the effective interface energy barrier height for n-type conduction, which is consistent with the previous study.[14] The larger drain current with increasing V_G is also consistent with the increase of the Fermi energy level of

graphene, which induces additional conduction electrons in the semiconductor and leads to a larger current at the junction with a lower effective energy barrier height. In order to identify the quality of the diode and to extract the energy barrier modulation at the graphene/N2200 junction, we measure the temperature-dependence of the output characteristics. We fit the experimental data by using the following equation,[14] $I_D = I_{sat}\left[exp\left(\frac{qV_D}{\eta k_B T}\right)\right]$, where I_{sat} is the zero-bias saturation current, k_B is the Boltzmann constant, T is the temperature, and η is the ideality factor. We can see from Figure 4(e) that the junction possesses a non-ideal diode behavior with an ideality factor η in the range of 3.5 to 10. The strong deviation from an ideal diode can be attributed to tunneling dominated transport at the graphene/N2200 interface as well as to multi-step tunneling from graphene to Al through the ~90 nm thick N2200 channel. The strong non-ideal diode behavior could also be associated to the charge recombination at the interface trap states similar to a p-n junction diode.[43] Finally, we extract the effective energy barrier height (ϕ_B) by using the Richardson–Dushman thermionic emission equation,[14,44] $\frac{I_{sat}}{T^2} = AA^* exp\left(-\frac{q\phi_B}{k_B T}\right)$, where A is the junction area and A^* is the effective Richardson constant. Figure 4(f) shows the semi-log plots of I_{sat}/T^2 versus $q/k_B T$s at various V_G. ϕ_B is estimated from the linear dependence of the experimental data. The change in slope highlights that the energy barrier height has a clear dependence on V_G as can be seen in Figure 4(g).

The low interface energy barrier height at large gate voltages, determined to be 150 meV at V_G of 60 V, together with the diode's ideality factor varying from 7 to 10, is a conclusive fingerprint that electron tunneling is the basis behind low-resistance graphene contacts to the N2200 polymer.

Interestingly, the VOFET operates in the gate voltage range of ± 30 V (Figure 3), while the CNP of graphene is at a much higher gate voltage of ~99 V of V_G. Since the Fermi-level of graphene depends on the square root of the carrier density, its change with the gate voltage for high doping regimes will be significantly smaller than close to the CNP. The decrease of the effective energy barrier height as determined from the Richardson-Dushman equation seems to point out that the strong modulation of the effective electron activation energy is not due to the weak modulation of graphene's work function but rather to the bending of the energy levels of the N2200 coming from the weak-screening effect. Our experimental results confirm then that the weak field screening of graphene allows the electric field to reach the N2200 polymer and enable the VOFET operation. Thus, it is important to note that in these VOFETs, the transistor operation principle is fundamentally different from our earlier reported VOFETs [14] where the observed changes to the electric-field modulation of the energy-barrier was dominated by the change in Fermi level around the CNP of graphene.[10,44]

CONCLUSIONS

In conclusion, we demonstrate the integration of two-dimensional graphene electrodes and solution-processed organic semiconductor for both lateral and vertical device architectures, overcoming the performance and limitations of traditional noble metals. The general strategy presented here allows us to precisely determine the contribution of the electrode to the electronic transport, and to reach different transport regimes for vertical device operation. Our devices with N2200 polymer exhibit n-type transistor operation with a drain current modulation up to $>10^6$ for lateral and $>10^3$ for vertical geometries at room temperature. We obtain a maximum value of electron field-effect mobility of N2200 polymer in a lateral transistor of $\sim 1.06 \times 10^{-2}$ cm^2/Vs at

room temperature. In the vertical diode architecture, the effective energy barrier height modulation across graphene/N2200 interface is found to be around ~500 meV. Our systematic study indicates the weak field screening of graphene to be the dominating mechanism providing the vertical organic transistor operation, when compared to the work-function modulation. High-performance transistor operation combining both graphene electrodes and solution-processed polymers provides an avenue for future plastic electronic applications. The large-scale availability of CVD-grown graphene would enable a transition towards the development of high-performance graphene/polymer heterostructures with potential low-cost, easy fabrication and high production throughput.

METHODS

Hybrid graphene/N2200-based plastic transistors are fabricated in three steps for LOFETs and four steps for VOFETs. In the first step, graphene-FETs are fabricated and characterized before the spin-coating of the polymer. The second step consists on (hexamethyldisilizane) HMDS vapor priming of the oxide dielectric, followed by the spin coating of the N2200 polymer. The final fabrication step is the deposition of the top Al electrode to obtain the vertical transistor geometry. For the graphene-FET fabrication, a large-area high-quality CVD-grown graphene is carefully transferred onto a 1×1 mm^2 Si/SiO_2 (300 nm) substrate (as received from Graphenea S.A.). Several graphene stripes are protected by PMMA patterned by e-beam lithography and the rest of the graphene film is etched by argon/oxygen plasma. The Ti/Au (5/40 nm) contacts are evaporated at the two ends of each graphene strip. The graphene FET is then electrically characterized in a variable-temperature high vacuum probe station (Lakeshore) with a Keithley-4200 semiconductor analyzer. Variability of the charge neutrality point is improved by HMDS

vapor priming. After characterization, the N2200 polymer is spin-coated on the sample substrate for 60 s at 4000 rpm. We evaporated the residual solvent by keeping the sample in vacuum (10^{-6} mbar) overnight. Finally, as the top electrode for the vertical transistor, a 20-nm-thick Al layer is evaporated by thermal evaporation in the UHV chamber (base pressure < 10^{-9} mbar) at a rate of 0.6 Å/s (starting from a slower rate of 0.2 Å/s) through a shadow mask that provides an overlapping area of 20 × 300 μm^2 between the graphene strip and the top electrode. The devices are then quickly transferred to the variable-temperature probe station for further electrical measurements.

ASSOCIATED CONTENT

Supporting Information

The Supporting Information is available free of charge.

Notes

The authors declare no conflict of interest.

ACKNOWLEDGMENTS

We acknowledge C. Gonzalvez and A. Mateo-Alonso for providing the polymer solution. We also acknowledge financial support from the European Union 7th Framework Programme under the European Research Council (Grant 257654-SPINTROS) and the Marie Curie Actions (607904-13-SPINOGRAPH), from the Spanish Ministry of Economy under Project No.

MAT2015-65159-R, and from the Basque Government under Project No. PC2015-1-01. A. A. thanks the Basque government for the PhD fellowship PRE 2015-2-0139.

REFERENCES

1 S. R. Forrest, *Nature*, 2004, **428**, 911–918.

2 L.-L. Chua, J. Zaumseil, J.-F. Chang, E. C.-W. Ou, P. K.-H. Ho, H. Sirringhaus and R. H. Friend, *Nature*, 2005, **434**, 194–199.

3 H. Sirringhaus, *Adv. Mater.*, 2005, **17**, 2411–2425.

4 H. Yan, Z. Chen, Y. Zheng, C. Newman, J. R. Quinn, F. Dötz, M. Kastler and A. Facchetti, *Nature*, 2009, **457**, 679–686.

5 M. Caironi, M. Bird, D. Fazzi, Z. Chen, R. Di Pietro, C. Newman, A. Facchetti and H. Sirringhaus, *Adv. Funct. Mater.*, 2011, **21**, 3371–3381.

6 C. Liu, Y. Xu and Y.-Y. Noh, *Mater. Today*, 2015, **18**, 79–96.

7 S. Pang, H. N. Tsao, X. Feng and K. Müllen, *Adv. Mater.*, 2009, **21**, 3488–3491.

8 K. S. Novoselov, A. K. Geim, S. V. Morozov, D. Jiang, Y. Zhang, S. V. Dubonos, I. V. Grigorieva and A. A. Firsov, *Science*, 2004, **306**, 666.

9 H. Yang, J. Heo, S. Park, H. J. Song, D. H. Seo, K.-E. Byun, P. Kim, I. Yoo, H.-J. Chung and K. Kim, *Science*, 2012, **336**, 1140–1143.

10 W. J. Yu, Z. Li, H. Zhou, Y. Chen, Y. Wang, Y. Huang and X. Duan, *Nat. Mater.*, 2012, **12**, 246–252.

11 T. Georgiou, R. Jalil, B. D. Belle, L. Britnell, R. V. Gorbachev, S. V. Morozov, Y.-J. Kim, A. Gholinia, S. J. Haigh, O. Makarovsky, L. Eaves, L. A. Ponomarenko, A. K. Geim, K. S. Novoselov and A. Mishchenko, *Nat. Nanotechnol.*, 2012, **8**, 100–103.

12 S. Parui, R. Ruiter, P. J. Zomer, M. Wojtaszek, B. J. Van Wees and T. Banerjee, *J. Appl. Phys.*, 2014, **116**, 244505.

13 M. G. Lemaitre, E. P. Donoghue, M. A. McCarthy, B. Liu, S. Tongay, B. Gila, P. Kumar, R. K. Singh, B. R. Appleton and A. G. Rinzler, *ACS Nano*, 2012, **6**, 9095–9102.

14 S. Parui, L. Pietrobon, D. Ciudad, S. Vélez, X. Sun, F. Casanova, P. Stoliar and L. E. Hueso, *Adv. Funct. Mater.*, 2015, **25**, 2972–2979.

15 E. H. Huisman, A. G. Shulga, P. J. Zomer, N. Tombros, D. Bartesaghi, S. Z. Bisri, M. A. Loi, L. J. A. Koster and B. J. van Wees, *ACS Appl. Mater. Interfaces*, 2015, **7**, 11083–11088.

16 W. H. Lee, J. Park, S. H. Sim, S. B. Jo, K. S. Kim, B. H. Hong, K. Cho, *Adv. Mater.*, 2011, **23**, 1752-1756.

17 S. J. Kang, G.-Hyoung Lee, Y.-Jun Yu, Y. Zhao, B. Kim, K. Watanabe, T. Taniguchi, J. Hone, P. Kim, C. Nuckolls, *Adv. Funct. Mater.*, 2014, **24**, 5157-5163.

18 R. Moriya, T. Yamaguchi, Y. Inoue, S. Morikawa, Y. Sata, S. Masubuchi, T. Machida, *Appl. Phys. Lett.*, 2014, **105**, 083119.

19 Y.-Fu Lin, W. Li, S.-Lin Li, Y. Xu, A. A.-Ferreira, K. Komatsu, H. Sun, S Nakaharai, and K. Tsukagoshi, *Nanoscale*, 2014, **6**, 795-799.

20 Z. Zhu, I. Murtaza, H. Meng and W. Huang, *RSC Adv.,* 2017, **7**, 17387–17397.

21 F. Schwierz, *Nat. Nanotechnol.*, 2010, **5**, 487.

22 H. Hlaing, C. H. Kim, F. Carta, C. Y. Nam, R. A. Barton, N. Petrone, J. Hone and I. Kymissis, *Nano Lett.*, 2015, **15**, 69–74.

23 Y. Liu, H. Zhou, N. O. Weiss, Y. Huang and X. Duan, *ACS Nano*, 2015, **9**, 11102–11108.

24 D. Jariwala, T. J. Marks and M. C. Hersam, *Nat. Mater.*, 2017, **16**, 170–181.

25 Y.-J. Yu, Y. Zhao, S. Ryu, L. E. Brus, K. S. Kim and P. Kim, *Nano Lett.*, 2009, **9**, 3430–3434.

26 A. K. Geim and K. S. Novoselov, *Nat. Mater.*, 2007, **6**, 183–191.

27 D. E. Eastman, *Phys. Rev. B*, 1970, **2**, 1–2.

28 T. H. Bointon, G. F. Jones, A. De Sanctis, R. Hill-Pearce, M. F. Craciun and S. Russo, *Sci. Rep.*, 2015, **5**, 16464.

29 A. J. Ben-Sasson, Z. Chen, A. Facchetti and N. Tessler, *Appl. Phys. Lett.*, 2012, **100**, 263306.

30 R. Steyrleuthner, M. Schubert, F. Jaiser, J. C. Blakesley, Z. Chen, A. Facchetti and D. Neher, *Adv. Mater.*, 2010, **22**, 2799–2803.

31 K. Szendrei, D. Jarzab, Z. Chen, A. Facchetti and M. A. Loi, *J. Mater. Chem.*, 2010, **20**, 1317–1321.

32 A. Atxabal, S. Braun, T. Arnold, X. Sun, S. Parui, X. Liu, C. Gozalvez, R. Llopis, A. Mateo-Alonso, F. Casanova, F. Ortmann, M. Fahlman, L. E. Hueso, Adv. Mater., 2017. DOI: 10.1002/adma.201606901.

33 C. Di, D. Wei, G. Yu, Y. Liu, Y. Guo and D. Zhu, *Adv. Mater.*, 2008, **20**, 3289–3293.

34 L. Ma and Y. Yang, *Appl. Phys. Lett.*, 2004, **85**, 5084.

35 N. Stutzmann, R. H. Friend and H. Sirringhaus, *Science*, 2003, **299**, 1881–1884.

36 A. J. Ben-Sasson, E. Avnon, E. Ploshnik, O. Globerman, R. Shenhar, G. L. Frey and N. Tessler, *Appl. Phys. Lett.*, 2009, **95**, 213301.

37 B. Liu, M. A. McCarthy, Y. Yoon, D. Y. Kim, Z. Wu, F. So, P. H. Holloway, J. R. Reynolds, J. Guo and A. G. Rinzler, *Adv. Mater.*, 2008, **20**, 3605–3609.

38 B. Lüssem, A. Günther, A. Fischer, D. Kasemann and K. Leo, *J. Phys. Condens. Matter*, 2015, **27**, 443003.

39 J. S. Kim, B. J. Kim, Y. J. Choi, M. H. Lee, M. S. Kang and J. H. Cho, *Adv. Mater.*, 2016, **28**, 4803–4810.

40 H. Kwon, M. Kim, H. Cho, H. Moon, J. Lee and S. Yoo, *Adv. Funct. Mater.*, 2016, **26**, 6888–6895.

41 T. T. Baby, M. Rommel, F. von Seggern, P. Friederich, C. Reitz, S. Dehm, C. Kübel, W. Wenzel, H. Hahn and S. Dasgupta, *Adv. Mater.*, 2016. DOI: 10.1002/adma.201603858.

42 C.-J. Shih, R. Pfattner, Y.-C. Chiu, N. Liu, T. Lei, D. Kong, Y. Kim, H.-H. Chou, W.-G. Bae and Z. Bao, *Nano Lett.*, 2015, **15**, 7587–7595.

43 S. Vélez, D. Ciudad, J. Island, M. Buscema, O. Txoperena, S. Parui, G. A. Steele, F. Casanova, H. S. J. Van Der Zant, A. Castellanos-gomez and L. E. Hueso, *Nanoscale*, 2015, **7**, 15442–15449.

44 C. Ojeda-Aristizabal, W. Bao and M. S. Fuhrer, *Phys. Rev. B - Condens. Matter Mater. Phys.*, 2013, **88**, 35435.

Figures and Figure Caption

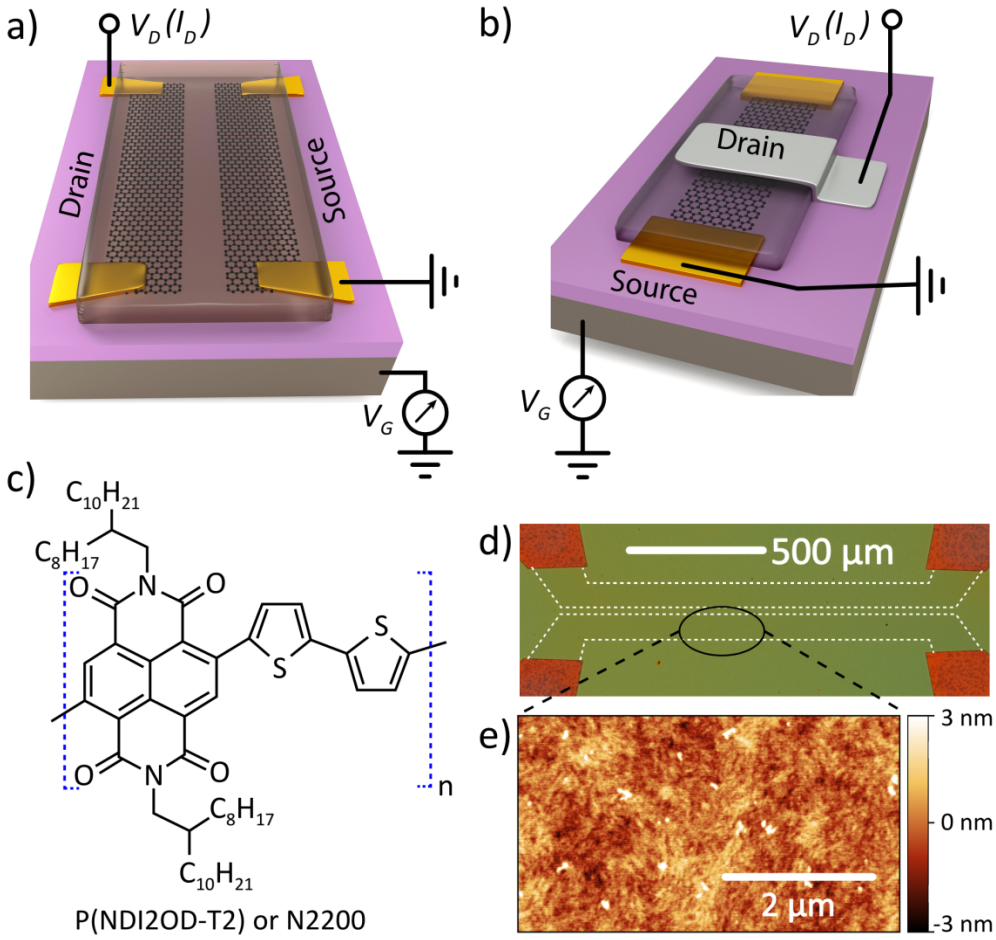

Figure 1. (a), (b) Sketch representing the graphene/N2200/graphene-based lateral organic field effect transistor (a) and the graphene/N2200/Al-based vertical organic field effect transistor (b). For the vertical device, the Al drain-electrode is evaporated on top of the 90-nm-thick N2200 channel. (c) Chemical structure of P(NDI2OD-T2) or N2200 polymer. (d) Optical microscope image of a lateral transistor. (e) Atomic force microscopy image of surface topography of the 90-nm-thick spin-coated N2200 polymer on top of graphene electrode. The root-mean-square (RMS) roughness is ~1 nm (peak-to-peak roughness is ~6 nm).

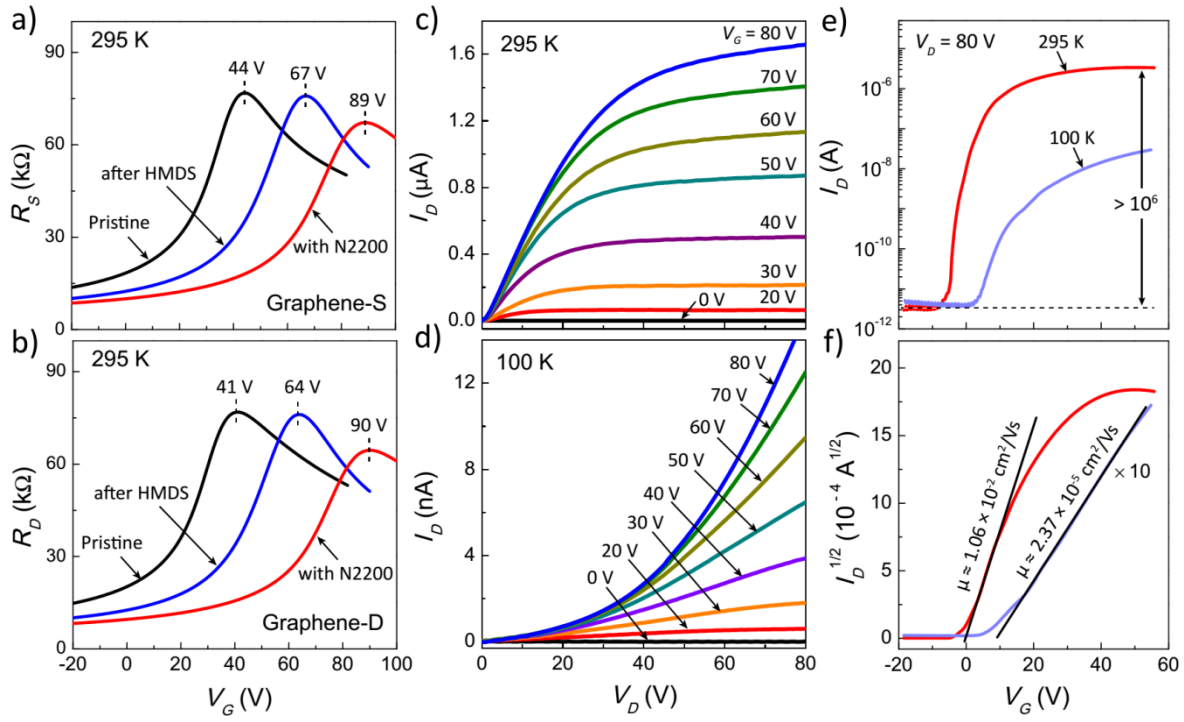

Figure 2. (a), (b) Electrical transport characteristics of the graphene electrodes used in the LOFET after electrode-shaping (black, pristine), after HMDS vapor priming (blue), and after N2200 spin coating (red) for graphene-source (a) and graphene-drain (b), respectively. The gate dependence of the graphene resistance is plotted at room temperature (RT) in all cases. (c), (d) Current–voltage output characteristics (I_D-V_D) of the LOFET as a function of different gate voltages at RT (c) and at 100 K (d), respectively. (e) Transfer plots of I_D - V_G of the LOFET at RT and at 100 K, with drain voltages of V_D = 80 V. (f) Square root of I_D as a function of V_G, from figure (e). The field-effect mobility (μ_{FE}) from the slope of the linear fit (black line) is calculated to be 1.06×10^{-2} at RT and 2.37×10^{-5} cm^2/Vs at 100 K.

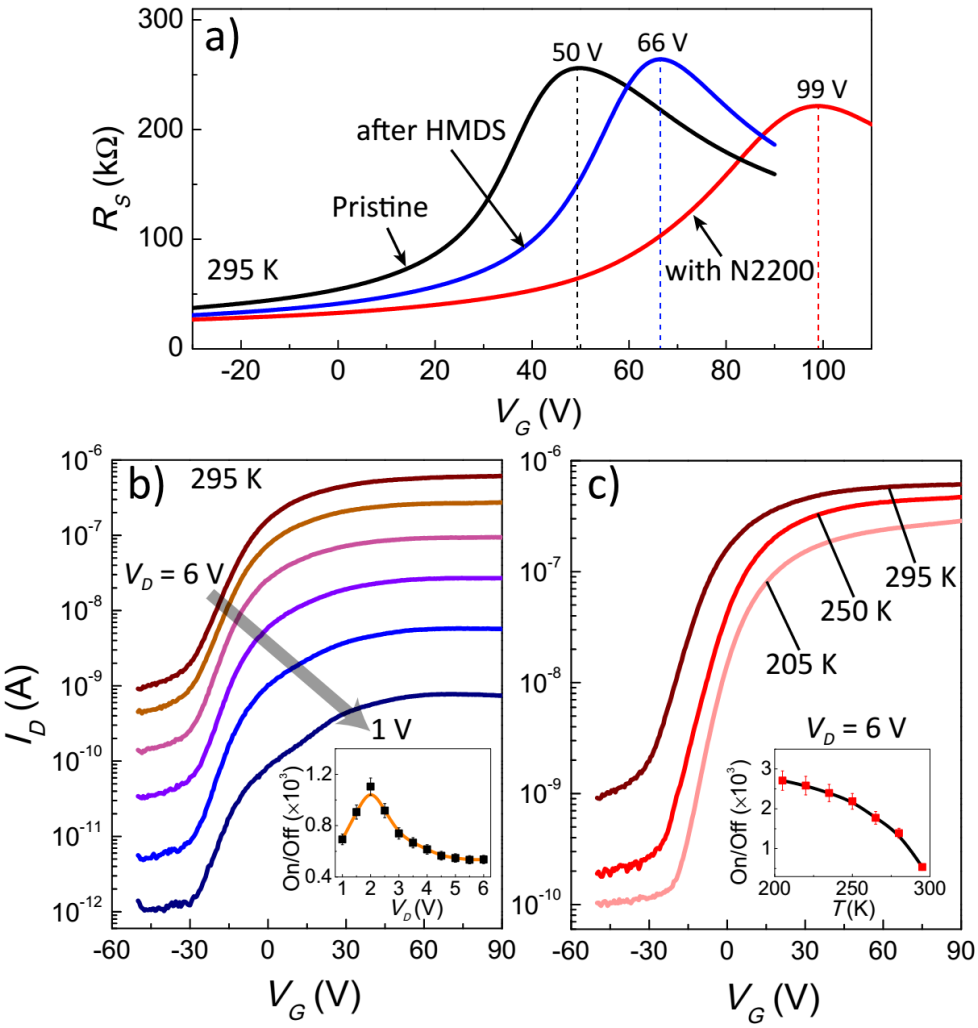

Figure 3. a) Gate dependence of the two terminal resistance of the graphene used as electrode for the VOFET operation, after shaping the graphene electrode (black, pristine), after HMDS-vapor treatment (blue) and then with spin-coated N2200 polymer (red). b) Positive-biased diode current versus V_G plots at several positive V_D with the step of 1 V. The corresponding current on/off ratio is shown in the inset. c) Positive-biased current versus V_G plots of the same diode at V_D of 6 V and at different temperatures from 295 to 205 K. The inset represents the corresponding change in current on/off ratio.

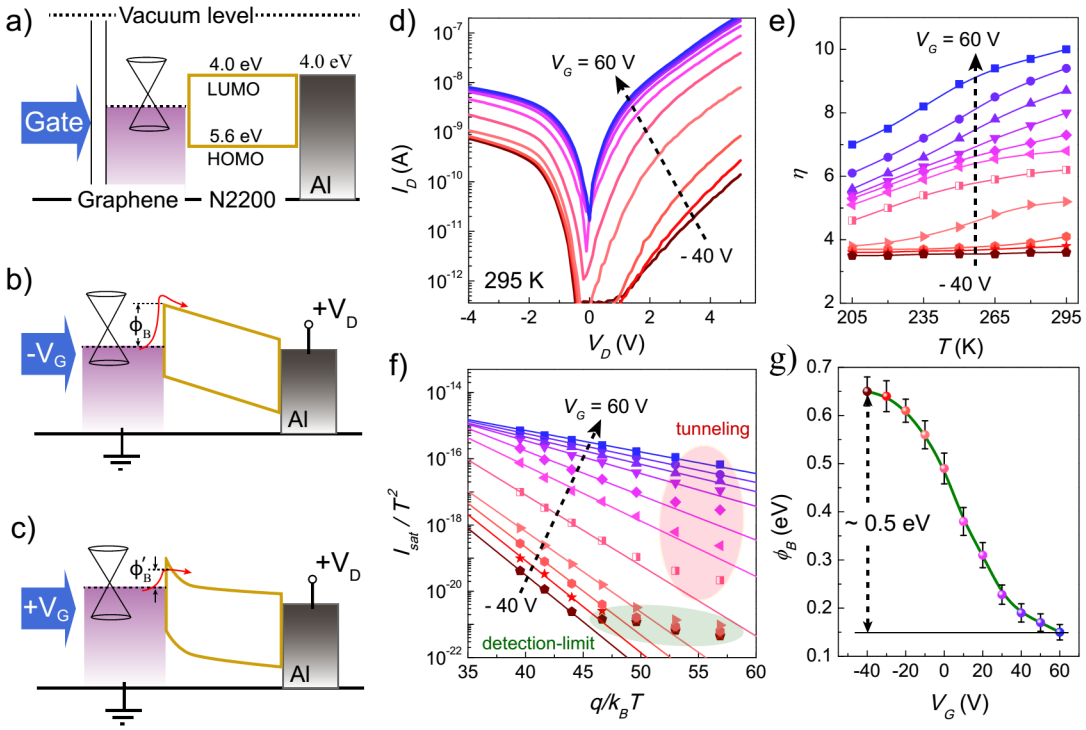

Figure 4. (a) Rigid band energy diagram of the graphene/N2200 heterojunction with Al top-drain contact. The effective barrier height at the N2200/graphene interface can be modulated according to the graphene Fermi energy shifts and also by the weak screening contribution for the change of gate voltage from negative (b) to positive (c), respectively. (d) Output characteristics of the VOFET (I_D-V_D) with different applied gate voltages V_G from -40 to 60 V with step of 10 V in semi-log scale. (e) The ideality factor, η and the corresponding zero-bias saturation current, I_{sat} is determined by fitting I_D at negative V_D (linear regime in semi-log scale) at various temperatures and gate voltages. (f) Interface energy barrier height determined from the I_{sat}/T^2 versus $q/(k_BT)$ plots. As indicated in the figure, the fitting shows discrepancies at low temperature due to: (1) the transition from thermally-activated process to temperature independent tunneling, and (2) the reduced current approaches to the gate leakage in the range of detection limit of the instrument. Gate modulated effective energy barrier heights are extracted from the slope (solid lines). (g) Effective energy barrier height plotted as a function of V_G.

TOC Graphic

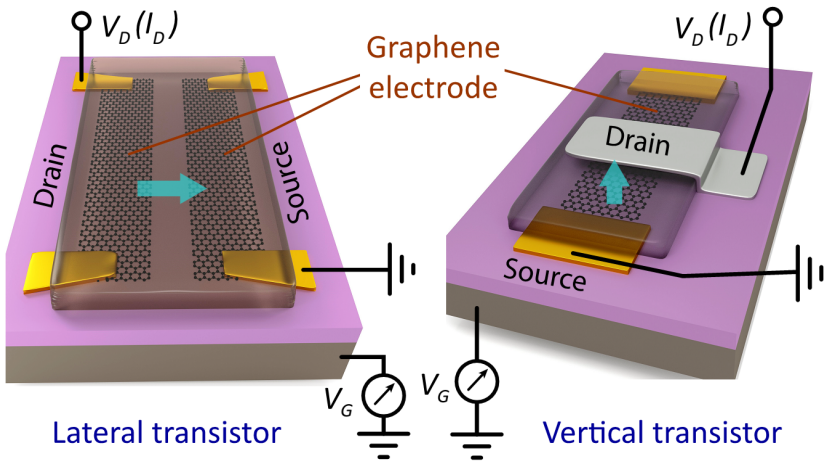

One sentence of text:

High-performance lateral and vertical organic field-effect transistors are demonstrated based on graphene electrodes and solution-processed N2200 polymer for advanced organic-electronics.